Seismic attenuation in the eastern Australian and Antarctic plates, from multiple ScS waves

Annie Souriau, Luis Rivera, Alessia Maggi, Jean-Jacques Leveque

Geophysical Journal International

Geophys. J. Int. (2012) **190,** 569–579 doi: 10.1111/j.1365-246X.2012.05501.x

Seismic attenuation in the eastern Australian and Antarctic plates, from multiple *ScS* waves

Annie Souriau,[1] Luis Rivera,[2] Alessia Maggi[2] and Jean-Jacques Lévêque[2]

[1] *CNRS, Institut de Recherche en Astrophysique et Planétologie, Observatoire Midi-Pyrénées,* 14 *Avenue Edouard Belin,* 31400 *Toulouse, France. E-mail: Annie.Souriau@irap.omp.eu*

[2] *CNRS, Université de Strasbourg,* 5 *rue René Descartes,* 67084 *Strasbourg Cedex, France*

Accepted 2012 April 6. Received 2012 April 4; in original form 2011 December 8

SUMMARY

The attenuation of seismic shear waves in the mantle beneath the eastern Australian and Antarctic plates is analysed using a large data set of multiple ScS_n waves, reflected n times at the core–mantle boundary and (n–1) times at the surface. The data are the transverse components of deep earthquakes from the subduction zones north and east of Australia, recorded at stations in Antarctica, Australia, Indonesia, New Caledonia and New Zealand. The data are filtered with narrow bandpass filters at five frequencies in the range 0.013–0.040 Hz. The ScS_{n+1}/ScS_n amplitude ratios of successive *ScS* phases are compared to the ratios computed for synthetic seismograms for the same paths and same focal mechanisms, to eliminate the effects of source radiation and geometric attenuation. The synthetic seismograms are computed from a summation of toroidal modes for the 1-D reference model PREM. The observed to computed spectral ratios appear consistent for similar paths. They reveal that the attenuation is not frequency dependent, that the contribution of scattering to attenuation is low, and that the PREM model is a valuable reference model for the study region at the considered frequencies. An inversion of the data at 0.026 Hz is performed to retrieve the quality factor Q in the upper mantle, in regions defined using *a priori* constraints inferred from seismic shear velocities. Q-values close to those of PREM are found beneath the Australian and Antarctic cratons, lower values beneath the Eastern Australian Phanerozoic margin, and very low values beneath the oceanic region between Australia and Antarctica, where ridges and a triple junction are present. The Australian–Antarctic Discordance along the South-Indian ridge appears as an exception with a Q-value close to those of stable continents. The highest Q-values are found beneath the subduction zones, a feature which is not apparent in global attenuation models possibly because of its narrow lateral extension, and because it extends at depths larger than those sampled by surface waves. Despite limitations due to the uneven distribution of the ScS_n bounce points at the surface and to the difficulty of collecting a large number of high quality data, our approach appears very promising. It is complementary to the more widely used determination of seismic attenuation using surface waves because it provides increased depth coverage, and a broader spectral coverage. It therefore has a considerable potential in future investigations of mantle structure and dynamics.

Key words: Body waves; Seismic attenuation; Seismic tomography; Antarctica; Australia.

1 INTRODUCTION

The structure of the mantle may be characterized by its seismic velocity, anisotropy and attenuation. This last parameter is the most difficult to retrieve, first because it can be frequency dependent, unlike seismic velocity and anisotropy, secondly because its determination relies on wave amplitudes, which are subject to numerous influences, and are thus more difficult to analyse systematically than traveltimes. Attenuation, in particular for shear waves, contains information on the thermal structure, fluid content (melt or water) and texture of mantle material (e.g. Artemieva *et al.* 2004), and is thus an important parameter for modelling mantle dynamics. Difficulties appear however for discriminating anelastic attenuation from the other physical processes that modify wave amplitudes, such as scattering and wave focusing and defocusing induced by velocity heterogeneities and anisotropy.

Anelastic tomography models are generally obtained at low frequencies from surface waveform amplitude data, or from normal

modes including overtones, and they provide images of the upper mantle. The use of low frequencies minimizes the contribution of scattering, but wave focusing by long wavelength heterogeneities introduces important biases, which must be corrected (Dalton & Ekström 2006, see also Romanowicz 1998, and Romanowicz & Mitchell 2007, for reviews). Retrieving anelasticity at higher frequencies requires the use of body waves, generally *S*, *SS* or *ScS*, but scattering may significantly contribute to amplitude variations and should be taken into account, as should a possible frequency dependence. *ScS* waves are particularly well suited to attenuation studies, because these phases sample the whole mantle and are well observed on the transverse components. They are generally analysed with reference to another phase, either the *S* phase if the lower mantle is investigated (Lawrence & Wysession 2006), or *sS* if the upper mantle is the subject of interest (Flanaghan & Wiens 1994), or a multiple *ScS* phase if the whole mantle is concerned. Multiple *ScS*-waves may still be observed on transverse component seismograms after up to four or five reverberations, due to their full reflection at both the surface and the core–mantle boundary, and to the absence of conversions to *P* or *SV*. They correspond to the high frequency spectrum of the Love wave higher modes, and provide complementary observations to surface waves in allowing the sampling of the deep mantle. Moreover, for nearly vertical paths, the source radiation is similar for all ScS_n rays and may be ignored when successive ScS_n phases are compared to each other.

Previous studies based on multiple *ScS* waves have estimated the shear quality factor Q from the decay of the spectral ratio of ScS_{n+1}/ScS_n (where ScS_n corresponds to n reflections at the core–mantle boundary) as a function of frequency, in a frequency range of about 0.005–0.06 Hz (e.g. Jordan & Sipkin 1977; Nakanishi 1979; Lay & Wallace 1983). However, large uncertainties in the spectral ratios at frequencies higher than 0.04 Hz introduce large errors on the slopes inferred from the decay rates. Here, we propose a slightly different method based on the comparison of the observed ratios with those obtained for synthetic seismograms. This method has several advantages: it directly takes into account source and propagation effects, it allows us to work at a single frequency, and it provides a good control on possible undesirable contributions due to nearby phases, scattered phases, high noise or strong focusing–defocusing effects. This method is applied to the Australian–Antarctic region, where global attenuation models retrieved from surface waves have a limited resolution, and where only few short period *ScS* wave studies have been performed (Choudhury & Dorel 1973; Frohlich & Barazangi 1980). The region is well sampled by high quality ScS_n waves thanks to the deep focus events of the nearby subduction zones, and to the availability of data from several permanent broad-band stations. Data from temporary stations deployed in Antarctica in the framework of the International Polar Year have also been used in this study.

2 DATA

Earthquakes and stations have been selected so that the bounce points of the ScS_n phases sample the Australian–Antarctic region, from latitudes -10° to -90° and from longitudes 70° to 190°. To obtain high quality observations of ScS_n up to $n = 4$, careful earthquake selection criteria have been applied. They first concern magnitudes ($M_b \geq 5.8$) and focal depths ($h \geq 100$ km) thereby limiting the useful focal regions to Tonga, Kermadec, New-Hebrides, Solomon Island and Indonesia. For Tonga events, we deepened the minimum focal depth to 400 km, to reduce the perturbing influence of local complex, strong upper mantle anomalies (Van der Hilst 1995). Secondly, stringent criteria have been imposed on the radiation pattern along the ScS_n rays toward the station: we imposed that the seismic moment be at least 0.5×10^{26} dyne cm (0.5×10^{19} N m), and that amplitude in the take-off direction of ScS_2 be at least 50% of the maximum amplitude in the radiation pattern. This last condition ensures that all the ScS_n rays leave the focus far from a nodal plane, since the take-off angles of ScS_n are close to each other (separations of less than eight degrees for ScS_2 and ScS_5, of less than five degrees for ScS_2 and *ScS*) even for the largest epicentral distances we considered (90°). Thus we ensure that the ScS_{n+1}/ScS_n ratios do not take very high or low values that could be unstable. Moreover, this radiation condition makes the modelling from synthetic seismograms relatively insensitive to uncertainties in moment tensor solutions. However, it does not guarantee a favourable radiation pattern for the depth phases $sScS_n$, therefore these phases have not been used.

We analysed data from the permanent stations of the FDSN consortium, and those from the temporary stations with public, non-restricted access. We also used data from the French-Italian station CCD, located inside the Antarctic continent at Concordia, Dome C (Lévêque *et al.* 2008; Maggi & Lévêque 2010), as well as data from temporary stations located around Dome C (Levêque *et al.* 2010). The ScS_5 phase arrives approximately 80 min after the earthquake origin time. We extracted about 100 min of signal for each earthquake to identify any multiple *ScS* and other body wave phases arriving from the major arc, which may contaminate the useful signal. In most cases, we selected the LH channel, as the sampling rate of 1 sps is convenient for the periods we consider ($T \geq 25$ s). We corrected horizontal components for instrument response and rotated them to obtain the transverse component, which carries the whole *ScS* signal if no strong anisotropy or heterogeneities are present. Figs 1(a) and (b) (top traces) give two examples of records at two different epicentral distances (26.6° and 46.5°) for a deep Tonga event (focal depth $h = 625$ km). ScS_n is well observed up to $n = 5$ for the shortest distance; we also note the similarity in shape of the successive ScS_n phases. The depth phases $sScS_n$ are also well observed up to $n = 4$. At 46.5°, the *sS* phase arrives about 30 s after *ScS*, which makes the use of *ScS* difficult at long period. The phase which arrives in the window of ScS_5 is larger than ScS_4 and has not the same shape as ScS_2, ScS_3 and ScS_4. It is therefore not ScS_5 but a shear wave arriving from the major arc. This example illustrates the difficulties inherent to phase identification and data processing of ScS_n. We developed and applied the automated data processing described later, which takes into account constraints on the distance and focal depth, and we subsequently visually checked the results of this processing for each path.

Our final data set comprised 68 earthquakes occurring between 1993 and 2010, recorded at 33 stations (Fig. 2a). The number of paths with useful observations is 361, after removal of ambiguous phases (Fig. 2b).

3 DATA PROCESSING

The method relies on applying identical processing to observed and synthetic seismograms. The quality factor may be obtained by comparing the observed and synthetic amplitude ratios. The instrument-corrected transverse components are narrow-band filtered around a frequency f_0, with a causal Butterworth filter. The use of a causal filter avoids the contamination of ScS_n by $sScS_n$. On the filtered record, we observe strong waveform similarity between two successive ScS_n

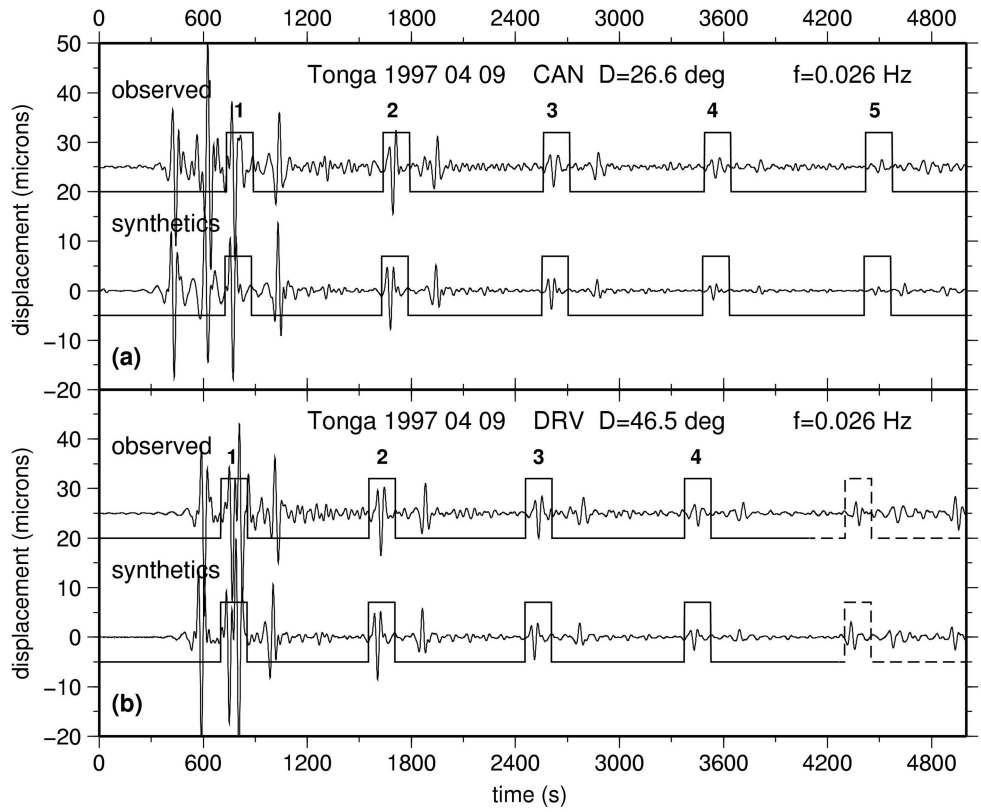

Figure 1. Two examples of observed and synthetic traces, for a deep Tonga earthquake (1997 April 09, depth = 625 km), recorded at Canberra (CAN) in Australia at epicentral distance 26.6° (a) and at Dumont d'Urville (DRV) in Antarctica, at epicentral distance 46.5° (b). Lower traces are the synthetics of transverse ground displacement, and top traces are the observed ones (shifted by 25 microns to avoid trace overlap). Traces are bandpass filtered around 0.026 Hz (period $T = 38$ s). The successive arrivals of ScS_n are indicated. Note that ScS_5 is not observed at DRV, due to the simultaneous arrival of phases from the great arc. Superimposed on the traces are the windows used for the automatic processing of the ScS_n phases.

phases. Windows of width $2/f_0$ are automatically generated around the theoretical arrival time of ScS_n (Fig. 1), and the amplitude ratios ScS_{n+1}/ScS_n are directly retrieved from the cross-correlation of the two signals inside these windows. This process is repeated for five frequency bands around 0.013, 0.020, 0.026, 0.033 and 0.040 Hz, to check for a possible frequency dependence of the attenuation.

The synthetic seismograms are computed with the Mineos software (Masters *et al.* 2011), which computes synthetic seismograms in a spherically symmetric non-rotating Earth by summing normal modes. Inputs are the 1-D Earth model and the centroid moment tensors. For an Earth model, we chose PREM (Dziewonski & Anderson 1981) with the ocean layer removed, because ScS_n reflects at the ocean floor at most of the reflection points (Fig. 2). We used focal parameters from the Global CMT Project (http://www.globalcmt.org; Dziewonski *et al.* 1981; Ekström 2007), and applied the same processing steps as for the observed traces. Fig. 1 (lower traces) shows that synthetic traces are very similar to the observed ones. The comparison of observed and synthetic traces helps identification of undesirable phases: the synthetic trace in Fig. 1(b) clearly confirms that the signal present in the ScS_5 window is not ScS_5, as it does not have the same shape as ScS_4. It also shows a stronger overlap of the *sS* and *ScS* phases than on the observed trace, possibly due to a slightly overestimated focal depth in the CMT solution. We consider the ScS_{n+1}/ScS_n ratios because they provide a more robust comparison between the observed and synthetic data than the absolute ScS_n amplitudes.

Fig. 3 gives an example of these ratios for the observed and for the synthetic seismogram of Fig. 1(b). They follow the same trend with frequency. However, we note that the observed and synthetic ScS_2/ScS ratios are very different from each other, probably because of the perturbing effect of *sS*. For the other phases, not contaminated by spurious arrivals, the ratios are roughly identical. The observed ScS_3/ScS_2 ratio is slightly larger than the synthetic one, whereas ScS_4/ScS_3 is closer to the synthetic prediction, suggesting the presence of lateral heterogeneities in attenuation along this path (for example a low Q at the ScS_2 surface bounce point).

More generally, the variability of ScS_{n+1}/ScS_n ratios may have several origins: the lateral variations of Q that we are looking for, but also perturbations of wave shape and wave amplitude due to scattering, lateral variations and frequency dependence of transmission/reflection coefficients at the interfaces, variations of radiated energy at the source for the different phases, and perturbation of ScS_n by other phases. As synthetics are computed in a radially stratified Earth, they will not be sensitive to lateral variations in Q, nor to scattering or anisotropy, but they will be affected as the real data by the radiation pattern at the source and by the undesirable phases, which come out of the modelling. Thus the comparison of the dispersion in the values of ScS_{n+1}/ScS_n for observations (obs) and for synthetics (syn) may be very informative in pointing out not only the possible heterogeneities in Q, but also the other origins of amplitude perturbations. Fig. 4 gives the histograms of these ScS_{n+1}/ScS_n ratios, as well as the histograms of the relative ratio $(ScS_{n+1}/ScS_n)_{\rm obs}/(ScS_{n+1}/ScS_n)_{\rm syn}$, for the data filtered at a central frequency of 0.26 Hz. The ScS_{n+1}/ScS_n ratios for the synthetics generally appear less scattered than for the observations. The dispersion for synthetics is however large for ScS_2/ScS and for ScS_5/ScS_4,

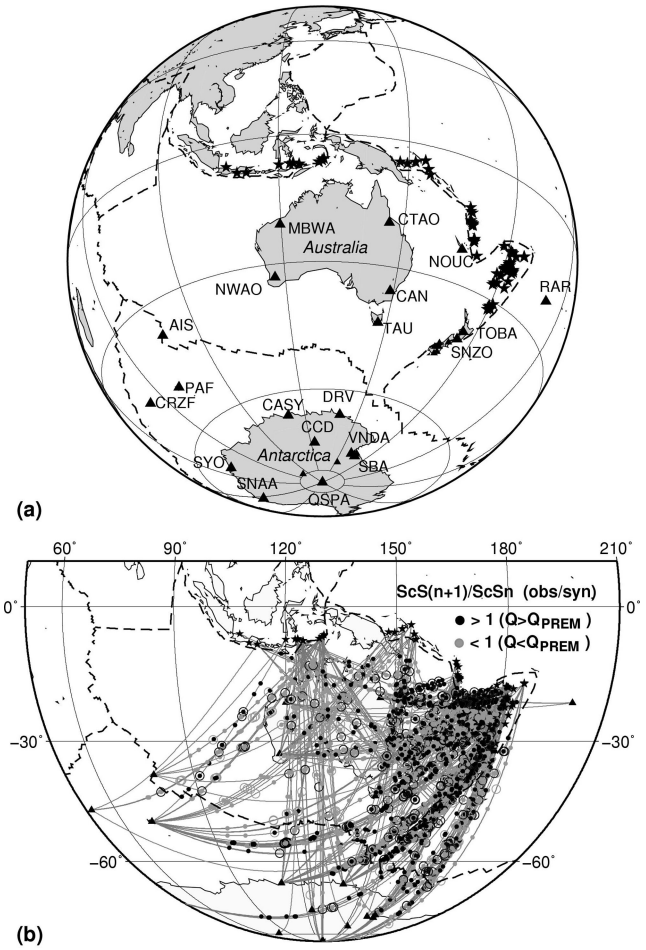

Figure 2. (a) Location of earthquakes (stars) and stations (triangles) used in this study (orthographic projection). Large triangles are the permanent stations with their codes, small triangles are temporary stations. Some temporary stations not visible on the figure are a few kilometres away from QSPA and CCD. Dashed lines are the plate limits of the Nuvel1 model (DeMets *et al.* 1990). (b) Projection at the surface (Equal area Mollweide projection) of the ScS_n paths, from earthquakes (stars) to stations (triangles). Bounce point are coloured according to the values of the ScS_{n+1}/ScS_n ratios for the path, compared to the ratios computed for PREM: black points correspond to ratios above 1 (mean Q-value along the path $> Q_{\mathrm{PREM}}$), grey points to ratios below 1 (mean Q-value $< Q_{\mathrm{PREM}}$). The same colour is given to all the reflection points of ScS_{n+1} and ScS_n for a given path. Filled points are for ScS_n when it appears at the numerator of ScS_n/ScS_{n-1}, open circles are for ScS_n when it appears at the denominator of ScS_{n+1}/ScS_n (the location is the same but the mean Q-value and hence the colour could be different).

due to the contamination by nearby phases and, especially for ScS_5, by phases arriving from the great arc. For ScS_3/ScS_2 and ScS_4/ScS_3, the ratios are close to 0.45, which reflects the mean amplitude decay of the wave during a round trip from the surface down to the core–mantle boundary and back to the surface.

As for the synthetics, the observed ScS_3/ScS_2 and ScS_4/ScS_3 ratios display the sharpest distributions and are thus considered to be the most reliable measurements. Curiously, the mean value of observed ScS_{n+1}/ScS_n increases when n increases from 1 to 4 (Fig. 4a), possibly because the relative influence of the heterogeneities near the slabs fades out when long, multiple paths are considered. The geographic distribution of the anomalies (Fig. 2) and the coherency for similar paths (Fig. 5), indicate that there is some tectonic-related information in the data. Comparison of the ratios obtained for observed and synthetic data (Fig. 4c) shows that the most probable relative ratio is close to 1, indicating that PREM is globally a good model for attenuation at the considered frequency.

4 RETRIEVING Q FROM THE AMPLITUDE RATIOS: METHOD

The amplitude A_k of the phase ScS_k for a given earthquake recorded at a given station may be expressed as

$$A_k = A_0(M_0)\,\mathcal{R}_k(M,i,\varphi)\,g(D,h)\exp(-\pi f t/Q), \quad (1)$$

where $A_0(M_0)$ is the amplitude at the source for seismic moment M_0, $R_k(M,i,\varphi)$ is the radiation pattern which depends on the seismic moment tensor M, the take-off angle i and the azimuth φ, $g(D, h)$ is the geometric spreading which depends on the distance D and on the focal depth h, f is the frequency, t the propagation time of the wave and Q the shear quality factor. More precisely, t/Q corresponds to the integral $\int(\mathrm{d}t/Q)$ along the ray.

Eq. (1) is applied to observed and synthetic signals, and we compute the amplitude ratios of ScS_{n+1} and ScS_n (respectively A_2 and A_1), assuming the radiated amplitude R_k is the same for the two phases. The observed-to-synthetic ratio R may be written as

$$\begin{aligned} \mathrm{R} &= \mathrm{Ln}\left[(A_2/A_1)\,\mathrm{obs}/(A_2/A_1)\,\mathrm{syn}\right] \\ &= -\pi f\,(t_2 - t_1)\,(1/Q\mathrm{obs} - 1/Q\mathrm{syn}), \end{aligned} \quad (2)$$

where t_2 and t_1 are the propagation times of ScS_{n+1} and ScS_n, respectively. Dividing the ratios obtained for the real traces by the ratios obtained for synthetics is equivalent to correcting the observations for the influence of distance, depth and focal mechanism.

If Q is not frequency dependent, R is linearly dependent on frequency f. Moreover, if the path samples a structure identical to PREM, R is 0 at all frequencies. Positive or negative slopes for a

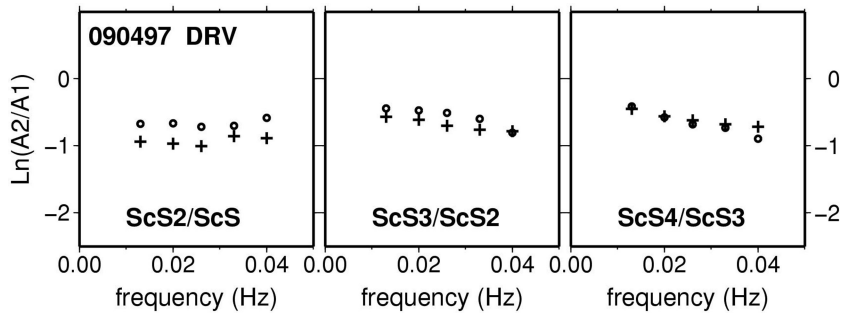

Figure 3. An example of ScS_{n+1}/ScS_n ratio for a deep Tonga event recorded at DRV in Antarctica. Ln (A_2/A_1) is plotted at five frequencies (A_2 is the amplitude of ScS_{n+1}, A_1 the amplitude of ScS_n). Circles represent data, crosses represent synthetics. Note the good general agreement between observations and synthetics. The poorer agreement for ScS_2/ScS is probably due to contamination of ScS by sS.

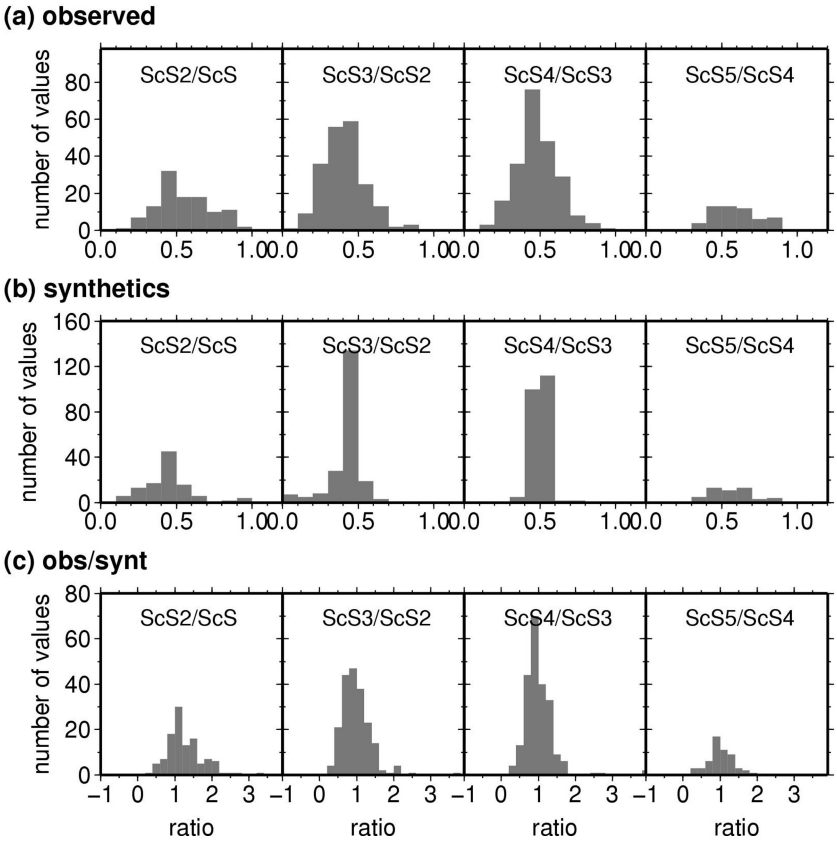

Figure 4. Histograms of ScS_{n+1}/ScS_n ratios for (a) data and (b) the corresponding synthetics. (c) Histograms of the ratios $(ScS_{n+1}/ScS_n)_{\rm obs}/(ScS_{n+1}/ScS_n)_{\rm syn}$.

given path denote a mean Q in the mantle larger or smaller than $Q_{\rm PREM}$, respectively. A frequency dependence of Q would induce a curvature in the $R(f)$ plots, in addition to the slope.

Some simplifications need to be made to pose an inverse problem, which can be resolved with our limited data coverage. As the multiple *ScS* rays propagate nearly vertically in the mantle, it will be difficult to separate the respective contributions of the upper mantle and lower mantle. We shall assume that Q does not exhibit significant lateral variations in the lower mantle, in agreement with previous studies (e.g. Flanaghan & Wiens 1994). We shall therefore ascribe all the amplitude variations to the upper mantle beneath the ScS_n reflection points at the surface. This point will be discussed in more detail later. To simplify the problem further, we consider that the differential propagation times of ScS_{n+1} and ScS_n in the upper mantle are independent of the epicentral distance. The time error induced is less than 3 per cent for the distance range we consider.

Using these simplifications, relation (2) may be re-expressed as

$$\begin{aligned} \mathrm{R} = &-2\pi f[t_{\rm UM}(1/Q_{\rm UM}\mathrm{obs} - 1/Q_{\rm UM}\mathrm{syn}) \\ &+ t_{\rm LM}(1/Q_{\rm LM}\mathrm{obs} - 1/Q_{\rm LM}\mathrm{syn})], \end{aligned} \tag{3}$$

where $t_{\rm UM}$, $t_{\rm LM}$ are the vertical, one way, traveltimes of the S-wave in the upper and lower mantle, respectively, and $Q_{\rm UM}$, $Q_{\rm LM}$ the mean quality factors in the upper and lower mantle, respectively. From this relation, we infer that a $Q_{\rm UM}$ or $Q_{\rm LM}$ model different from the one used for the synthetics will result in a slope of $R(f)$.

Assuming that the lower mantle Q-model is correctly represented by PREM, we obtain

$$\begin{aligned} \mathrm{R} &= \mathrm{Ln}\,(A_2/A_1)\,\mathrm{obs} - \mathrm{Ln}\,(A_2/A_1)\,\mathrm{syn} \\ &= -2\pi f t_{\rm UM}\,(1/Q_{\rm UM}\mathrm{obs} - 1/Q_{\rm UM}\mathrm{syn})\,. \end{aligned} \tag{4}$$

The values of $Q_{\rm UM}$ are laterally assigned to the surface reflection points of the two phases involved in the amplitude ratio: For ScS_2/ScS, they are assigned to the reflection point of ScS_2 (one point), for ScS_3/ScS_2 they are assigned to the reflection points of ScS_3 and ScS_2 (three points), for ScS_4/ScS_3, to the reflection points of ScS_4 and ScS_3 (five points), and so on.

For example, for ScS_4/ScS_3:

$$\begin{aligned} \mathrm{R} = &-2\pi f t_{\rm UM}\,(1/Q\mathrm{obs}_{41} + 1Q\mathrm{obs}_{42} + 1/Q\mathrm{obs}_{43} \\ &- 1/Q\mathrm{obs}_{31} - 1/Q\mathrm{obs}_{32} - 1/Q_{\rm UM}\mathrm{syn})\,, \end{aligned} \tag{5}$$

where $Q\mathrm{obs}_{41,\,42,\,43}$, and $Q\mathrm{obs}_{31,\,32}$ denote the Q-values in the upper mantle at the three reflection points of ScS_4 and at the two reflection points of ScS_3, respectively, and $Q_{\rm UM}$syn corresponds to the mean Q-value in the upper mantle for PREM.

5 RESULTS

5.1 Spectral ratios

Since synthetics have been computed with PREM (Dziewonski & Anderson 1981), we also used the Q-value of PREM to compute $\int(\mathrm{d}t/Q)$ in the lower mantle for use in relation (3). Fig. 5 shows the values obtained for R at different frequencies for ScS_2/ScS, ScS_3/ScS_2 and ScS_4/ScS_3, for paths sampled by different earthquake-station pairs. We observe consistent results for similar paths. Moreover, the trends are all approximately linear, suggesting that Q is not frequency dependent. The slopes are generally different from zero, indicating that along these paths the mean Q differs from $Q_{\rm PREM}$. Note however that results for ScS_2/ScS are very scattered, as already seen in the histograms of Fig. 4(a).

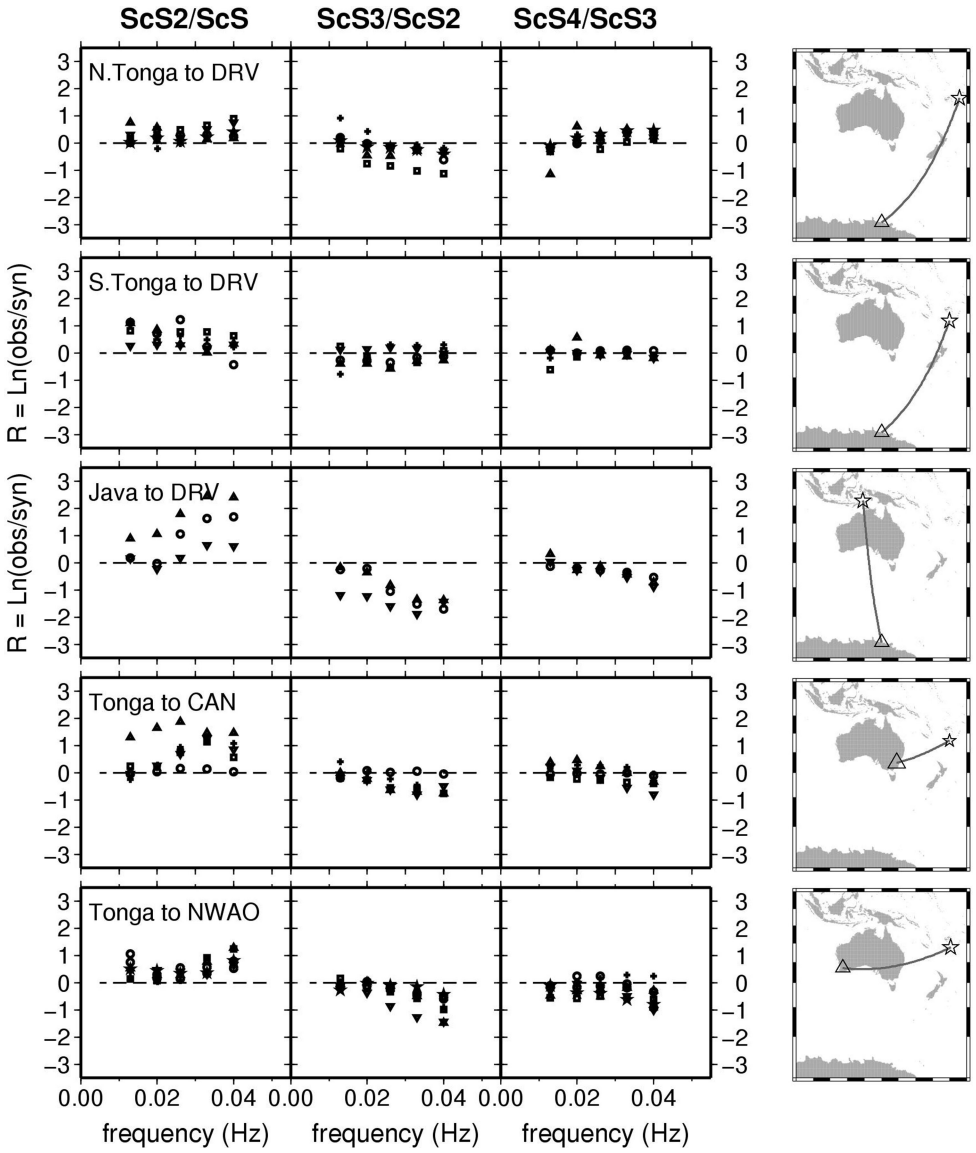

Figure 5. A logarithmic scale representation of the relative ratios $(ScS_{n+1}/ScS_n)_{\rm obs}/(ScS_{n+1}/ScS_n)_{\rm syn}$ as defined in eq. (2), for a selection of paths. Paths are mapped on the right with a triangle representing the station and a star representing the epicentres. For each path, the different symbols in the relative ratio plots correspond to different events. ScS_5/ScS_4 is not shown. The horizontal dashed line corresponds to PREM. The linear trends in relative ratios indicate that Q is globally independent of frequency. A positive (respectively negative) slope corresponds to a Q-value larger (respectively smaller) than the PREM one. Note the coherence of results for the different events corresponding to a same path, and the variations of slopes between paths and between different multiple ScS_n waves.

Since relation (3) depends on the lower mantle model used for synthetics, it is important to estimate how much a mismodelling of the lower mantle can impact the upper mantle Q-model. Here we discuss only the influence of the 1-D lower mantle Q-model on the values of R. PREM's lower mantle is very simple, with a constant value of 312 from 670 km depth to the core–mantle boundary. From normal modes, Durek & Ekström (1996) obtain a constant Q-value of 355 in their QL6 model. From ScS/S spectral ratios, Lawrence & Wysession (2006) propose a lower mantle model (QLM9) with radial variations of Q, they imposed $Q = Q_{\rm PREM}$ in the upper mantle. For these three models, $\int({\rm d}t/Q_{\rm LM})$ is respectively 1.03 s, 0.91 s and 0.94 s for a single vertical S-wave path in the lower mantle, assuming that the velocity model the same. From relation (3), we get the perturbation of R due to a perturbation of the lower mantle Q-model

$$\delta R = -2\pi f \delta \left(t_{\rm LM}/Q_{\rm LM}{\rm syn}\right). \quad (6)$$

If the real lower mantle is close to the model of Durek & Ekström (respectively to the model of Lawrence & Wysession), the use of PREM for the synthetics will result in a positive slope ${\rm d}R/{\rm d}f = 0.75$ s (respectively 0.57 s), which has an almost negligible contribution to the slopes (either positive or negative) observed in Fig. 5. At the central frequency of 0.026 Hz, this bias due to an incorrect lower mantle Q-model will result in an average decrease of the quality factor $Q_{\rm UM}$ of 16 (respectively 12). Note however that this bias will be the same for all paths, so that lateral variations of Q in the upper mantle will not be affected by the choice of the lower mantle 1-D reference model.

5.2 Inversion

We aim to evaluate our multiple *ScS* method for retrieving the seismic attenuation of a given region. Because of the limited number of bounce points, we have chosen to impose on the inversion some *a priori* information related to tectonic setting. We start by considering a five region model (Fig. 6) which follows the variations of shear velocity as given by the tomographic *S*-velocity models derived from surface waves (Debayle & Kennett 2000a; Danesi & Morelli 2001; Sieminski *et al.* 2003; Debayle & Sambridge 2004; Lekić & Romanowicz 2011). This choice is justified by the strong correlation found by previous studies between *S*-velocities and attenuation in the upper mantle (e.g. Dalton & Ekström 2006). Four of the regions (Fig. 6) contain a significant number of independent bounce points, a necessary condition for the inversion to be stable. Regions 1 and 2 correspond to Precambrian and Phanerozoic Australia, respectively, region 3 corresponds to the Fiji, Tonga, Vanuatu and New-Zealand deep subduction zones, region 4 corresponds to the ocean outside these subduction zones, and region 5, less well-sampled than the others, corresponds to the East Antarctic craton.

The inversion has been performed using the singular value decomposition method. We have considered three sets of data: (1) the whole set of relative ratios, (2) only the ScS_3/ScS_2 and ScS_4/ScS_3 relative ratios, (3) only the ScS_4/ScS_3 relative ratios. A few relative ratios far from the expected value of 1 have been removed from all data sets (i.e. values above 2.5 or below 0.4). They generally correspond to measurements made at stations of southern Indian Ocean (PAF, AIS, CRZF) where the microseismic noise is high, or at temporary stations with a weak s/n ratio, or in some cases to probable ScS_n contamination by unidentified phases. The number of bounce points is 564 for data set 1, it decreases to 402 for data set 2 and to 207 for data set 3. The data are of better quality when ScS_2/ScS and ScS_5/ScS_4 are omitted (i.e. for data sets 2 and 3), as shown in Fig. 4, and the inversion becomes more stable. The variance reduction is maximum when only ScS_4/ScS_3 are considered (data set 3), but the smaller number of bounce points makes the results very dependent on the exact location of the boundaries of the *a priori* regional model. The most stable solution is obtained with data set 2. Regardless of the data set, however, the data variance reduction with respect to PREM does not exceed 13 per cent. This variance reduction represents only a modest improvement to the attenuation model described by PREM, but is not surprising since we force our model to have only five, homogeneous regions.

Table 1 gives the results obtained with data set 2 when the first three eigenvalues among the five are kept. These three eigenvalues carry 93 per cent of the energy. The fifth eigenvalue is very small (less than 4 per cent of the largest one) and is likely to bring only noise into the model. The fourth eigenvalue is larger, but including it gives a solution, which strongly varies with the region boundaries, and generally results in an un-physical model that strongly violates our *a priori* knowledge of the structure. The 2σ-confidence level on Q as given by the inversion is of the order of 30, however this probably underestimates the real error bars. In Table 1, we give the Q-values for our five-region inversion (straight characters) obtained by assuming that only the upper mantle is responsible for lateral variations in attenuation, and that the lower mantle is correctly represented by PREM. We consider successively the whole upper mantle (670 km), the uppermost 400 km or the uppermost 220 km. For these three depth ranges, the mean values of Q^{-1} for PREM are 7.53×10^{-3}, 7.91×10^{-3} and 8.66×10^{-3}, respectively (i.e. Q-values of 133, 126 and 115, respectively). For comparison with previous results inferred from surface waves, Table 1 also gives $(Q^{-1} - Q^{-1}_{\mathrm{PREM}})$ and $\mathrm{d}Q/Q$ when concentrating all the attenuation heterogeneity in the uppermost 220 km, which is the main depth range of sensitivity of surface waves.

The results are globally consistent with what could be anticipated from tectonic arguments, with higher Q-values found beneath the cratons (West Australia and East Antarctica) and beneath the subduction zones, and lower values found beneath East Australia and the oceans. For all three inversions, we find that cratons have PREM-like Q-values, subduction zones have Q-values that are higher than

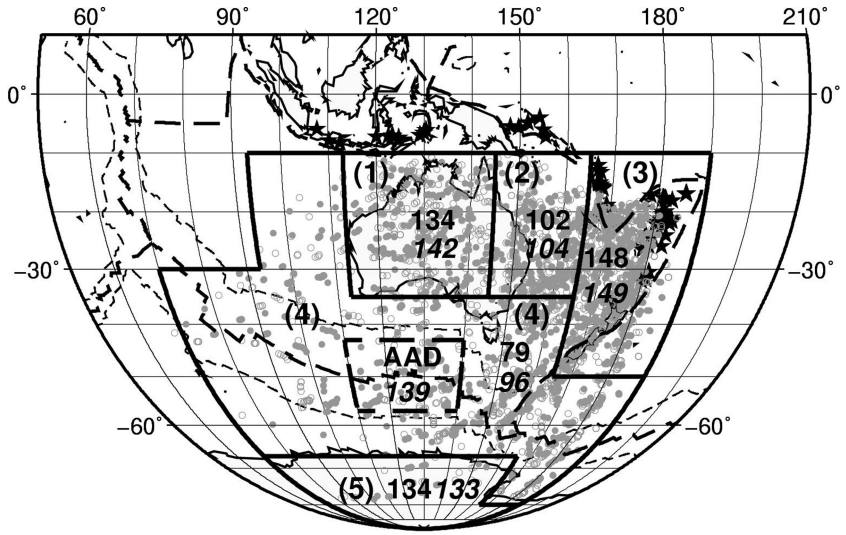

Figure 6. The five tectonic regions used for the inversion, and a distinct sixth region (with dashed contours) introduced to check the structure beneath the Australian–Antarctic Discordance (AAD). The values given in straight are the mean quality factors for the uppermost 670 km in each of the five regions, assuming that the lower mantle has the quality factor of the 1-D PREM model (Dziewonski & Anderson 1981). Those in italics correspond to the inversion that includes the AAD region. Grey dots are the surface bounce points of ScS_3 and ScS_4 used in this inversion, open circles are those of ScS_2 and ScS_5 (not used here). Thick dashed lines are plate boundaries (DeMets *et al.* 1990), thin dashed lines correspond to age 30 Ma.

Table 1. Results of inversion. In straight characters: results obtained for five tectonic regions defined from the *S*-velocity variations (Fig. 6). The inversion is performed using the ScS_3/ScS_2 and ScS_4/ScS_3 spectral ratios. The mean shear quality factor Q in the upper mantle is given down to three depths (670 km, 400 km, 220 km), assuming it takes PREM values at larger depths. Values in italics are those obtained when a sixth region corresponding to the Australian–Antarctic Discordance (AAD) is introduced. The two last columns refer to the inversion for the uppermost 220 km, and are shown to facilitate comparison with surface-wave attenuation studies.

Region	Q_{670}	Q_{400}	Q_{220}	$(Q^{-1}-Q^{-1}_{\rm PREM})_{220}$	$(\mathrm{d}Q/Q)_{220}$ (per cent)
Waterless PREM	*133*	*126*	*115*		
1-W-Australia	134 (*142*)	128	118	-0.18×10^{-3}	+2
2- E-Australia	102 (*104*)	87	67	6.20×10^{-3}	−58
3- Subduction zones	148 (*149*)	150	154	-2.20×10^{-3}	+33
4- Ocean (*AAD*)	79 (*96*) (*139*)	63	44	14.0×10^{-3}	−62
5- E-Antarctica	134 (*133*)	128	118	-0.18×10^{-3}	+2

PREM, and East Australia and the oceans have Q-values that are notably lower than PREM. If we consider the whole upper mantle (670 km), we find a mean quality factor $Q = 134$ beneath West Australia and East Antarctica, that decreases to $Q \sim 100$ beneath East Australia, which corresponds to the Phanerozoic margin of the continent. Q is close to 80 in region 4 for this inversion, which is a low value for an ocean. We note, however, that a large number of bounce points are close to the ridges, with an important number of points close to the Macquarie triple junction, which may contribute to lowering our retrieved Q. The highest value ($Q \sim 150$) is obtained beneath the subduction zones, and is consistent with the presence of very deep, fast shear wave velocities, in particular beneath the Fiji-Tonga region (Van der Hilst 1995; Bijwaard *et al.* 1998). The average of our Q-values is somewhat different from the mean $Q_{\rm PREM}$ value for the upper mantle, and may be explained by the fact that we sample only a small part of the world. However, we believe the relative variations of Q within our study region to be significant.

6 DISCUSSION

The stability of our Q-results and their coherency with the tectonic pattern inferred from seismic velocities gives credit to our approach based on multiple *ScS*-wave analysis. This method thus appears as a very interesting and complementary method with respect to surface wave analyses commonly used to infer attenuation in the mantle. In particular, it allows to sample a deeper part of the mantle, and to investigate higher frequencies. We discuss hereafter some points related to the method and to the results.

6.1 Frequency dependence of Q

We have found that, in the frequency range considered (0.013–0.040 Hz), our data do not require a frequency dependent quality factor (Fig. 5). This result, obtained from a large data set, is robust. It is consistent with previous results based on the decay of ScS_n spectral ratios, obtained for various regions of the world (e.g. Jordan & Sipkin 1977; Nakanishi 1979; Lay & Wallace 1983, 1988). These results also imply that scattering makes only a moderate contribution to attenuation, otherwise it would generate frequency dependent quality factors (irregularities in the slopes in Fig. 5), depending on the size of the heterogeneities. At higher frequencies (0.6–6 Hz), Cheng & Kennett (2002) found for the Australian lithosphere a rather weak frequency dependence in cratonic areas, but a more complex attenuation beneath the tectonic regions of Eastern Australia. The interest of *ScS* is to permit the sampling of a frequency range, which is intermediate between surface waves and regional body wave tomography.

6.2 Influence of the lower mantle

We have ascribed all the regional variations of Q to the upper mantle. In the literature, the low degree of lateral variation of Q in the lower mantle is mostly inferred from indirect arguments, such as the low variance of radial Q-models, the high viscosities in the lower mantle, and the low degree of lateral variation in seismic shear velocity. To our knowledge, to date no 3-D Q-model is available for the lower mantle. Only a degree-two pattern has possibly been identified (Romanowicz 1998). Reid *et al.* (2001) retrieve Q-values down to 1100 km, and show that lateral heterogeneity decreases significantly beneath 600 km depth. At greater depth, although some 3-D images reporting very large (probably unrealistic) lateral variations of Q have been referred to in a discussion about the presence of water in the lower mantle (Lawrence & Wysession 2006), the corresponding model is as yet unpublished. We have chosen the conservative approach and follow the general consensus in the literature by assuming that the lower mantle contributes only marginally to our observations.

6.3 Adding a region for the Australian–Antarctic Discordance

Our inversion is restricted to five regions and to a single layer (the upper mantle). Seismic velocity tomography reveals complex structures with short wavelength heterogeneities in the Australian continent (Fishwick & Reading 2008; Fichtner *et al.* 2010) as well as in the oceans (Lekić & Romanowicz 2011). We also ignored anisotropy, which may be relatively strong in some places (Debayle & Kennett 2000b; Reading & Heintz 2008; Fichtner *et al.* 2010). Thus our model is far from reproducing the complexity of the structure as revealed by seismic velocities. In particular, we have disregarded the Australian–Antarctic Discordance (AAD), which is a very anomalous feature along the Southeast Indian ridge (Gurnis *et al.* 1998; Whittaker *et al.* 2010), with high seismic velocities in the uppermost 120 km of the mantle (Ritzwoller *et al.* 2003). An inversion adding a sixth region related to the AAD (Fig. 6) has been attempted. The results obtained with three eigenvalues are presented in italics in Table 1. A high quality factor is obtained for this region,

with a value close to that of cratons. The Q-values for the other regions remain unchanged, except for region (4), where Q increases slightly. This unexpected increase indicates that Q is not strongly constrained in this rather heterogeneous region. Unfortunately, not enough data are available to perform an inversion in regions based on ocean age.

6.4 Comparison with previous Q-results from body wave analyses

Keeping in mind our limited geographic resolution, we now compare our results with the few previous regional Q-results available for Australia and East Antarctica and also with global models of seismic attenuation. Most of the regional results obtained from *ScS*-wave analyses concern structures, which lie at the boundary of the region we investigated. The quality factor Q has been found to be significantly larger than average beneath the South-East Pacific (Chan & Der 1988), and very large beneath the Ontong–Java Plateau (Gomer & Okal 2003). These values are consistent with the very high value we have found beneath the subduction zones in our region 3. A rather high Q has also been found beneath station DRV at Dumont d'Urville on the Antarctic margin (Choudhury & Dorel 1973). Frohlich & Barazangi (1980) have estimated Q in the lower mantle between Fiji-Tonga and Australia from a comparison of (*ScP*-*PcP*) and (*ScS*-*PcS*) waves, and obtain a value of 1050 at 1 Hz. This estimation justifies our assumption that most of the attenuation can be ascribed to the upper mantle, despite a longer path in the lower mantle: the contribution of the upper mantle to the global attenuation is close to 75 per cent.

At the global scale, only two studies based on the analysis of the body waves *SS*-*S* and *SSS*-*SS* (Bhattacharyya *et al.* 1996; Reid *et al.* 2001) can be compared to our results. Although Bhattacharyya *et al.* (1996) analyse only few data in our region of interest, they clearly detect the difference between Eastern Australia, with a low Q, and the rest of the continent, with a high Q. From a much larger data set, Reid *et al.* (2001) also observe a low Q beneath the Southeast Indian ridge, but their sampling of the subduction zones remains poor. In the depth range 100–300 km, they find that attenuation (Q^{-1}) decreases approximately by 6×10^{-3} beneath Western and Central Australia on one side, and the Eastern Australian margin on the other side. This decrease is remarkably consistent with what we observe (Table 1).

6.5 Comparison with previous Q-results from surface wave analyses

Most of the studies at the global scale rely on surface waves analyses, which mostly sample the uppermost 200 km of the mantle, and generally provide poor sampling of Antarctica. Most models reveal the same tendencies we have observed, though with a lower level of heterogeneity, and notably no Q-heterogeneity related to subduction zones, possibly because they are too narrow for Q-variations to be detected there (Billien *et al.* 2000; Selby & Woodhouse 2002; Gung & Romanowicz 2004; Dalton & Ekström 2006, for the most recent ones). Gung & Romanowicz recognize that the amplitudes of the lateral variations of Q are poorly constrained, due to the difficulty of extracting the weak Q-signal from the data. As the amplitude decay of body waves (such as multiple *S* or multiple *ScS*) is faster than for surface waves, the attenuation is a priori easier to retrieve from body waves. Dalton & Ekström (2006) inverted simultaneously the elastic and anelastic parameters, and took into account the effect of wave focusing on amplitudes. Their results reveal Q-contrasts similar to ours, but detailed comparison is difficult because the results are given not as a function of depth, but as a function of Rayleigh wave periods. Fichtner *et al.* (2010) used full waveform tomography to retrieve the Australian upper mantle structure. They obtain values of $\mathrm{d}Q/Q$ at 100 km depth of the order of 3 to 5 per cent in Western Australia, consistent with our value for $(\mathrm{d}Q/Q)_{220}$ (Table 1). In our region 2 (East Australia), where our results predict a rather strong attenuation $(\mathrm{d}Q/Q)_{220} = -58$ per cent), they obtain values ranging from about -5 per cent to the South to -30 per cent to the North, which is only one half of our mean value.

6.6 Origin of the regional variations of Q

Our results show that quality factor and seismic velocities vary with similar trends, which justifies a posteriori the regionalization we adopted for the inversion. In the continents, the lateral variations of the quality factor are clearly linked to the ages of the structure, with higher values in the Precambrian cratons of East-Antarctica and West-Australia than in the Phanerozoic structures of East-Australia, reflecting a difference in thermal state and lithospheric thickness (Debayle & Kennett 2000a; Sieminski *et al.* 2003; Fishwick *et al.* 2005). Beneath oceans, the Q-value we obtain is pushed toward low values by the large number of bounce points that occur in young ocean (age < 30 Ma) with warm lithosphere (Fig. 6). The AAD, on the other hand, is often associated with cold or depleted upper mantle, and its negative topography compared to the ridge is presumed to reflect a downwelling caused by a subducting Mesozoic slab (Gurnis *et al.* 1998; Whittaker *et al.* 2010) with high seismic velocities (Ritzwoller *et al.* 2003), which is consistent with our low attenuation (high Q) result. Finally, the high Q-value we find in our region 3 (subduction zones) denotes subducted material that remains cold even at large depths, due to the high rate of plate convergence in the region (about 10 cm yr^{-1}), and is in agreement with the results of seismic velocities (Van der Hilst 1995). However, an extension of the slab in the lower mantle would result in a decrease of the relative $\mathrm{d}Q^{-1}/Q^{-1}$ perturbation when we confine all the anomalies in the upper mantle.

7 CONCLUSION

We have presented a first attempt to use ScS_n amplitudes to retrieve the quality factor of the mantle at a regional scale, with a method based on the comparison of observed ScS_{n+1}/ScS_n ratios with synthetic ones. We find that cratons have PREM-like Q-values, subduction zones have Q-values significantly higher than PREM, and east Australia and the oceans have Q-values notably lower than PREM, if one excludes the region of the Australian–Antarctic Discordance, where Q is high. The method shows considerable promise although it may prove difficult to obtain a sufficiently large number of good observations that sample a study region evenly. In a region such as Antarctica, where sampling by surface waves is poor, multiple *ScS* data may provide an important means of investigating the deep tectonic structure.

It seems clear that the use of ScS_n alone will not allow us to obtain an attenuation model at the global scale. However, if combined with surface wave analyses and with other body wave methods, it may help to increase the resolution at depth, and to broaden the frequency range over which attenuation is retrievable. Depth resolution and improved frequency range are particularly important to understand

the physical origins of attenuation at different depths, and to relate seismic velocity, anisotropy and attenuation to the global dynamics of the Earth.

ACKNOWLEDGMENTS

We warmly thank the seismic station operators and the scientists who make their data available to the wider scientific community. The facilities of the IRIS Data Management Center were used to collect waveforms and metadata. The data provided by IRIS derived from PASSCAL, POLENET, AGAP and the following FDSN networks: GE, GT, II, IM, IU, PS, GEOSCOPE. Funding and logistical support for the French Antarctic seismic stations at Dumont d'Urville and Concordia and for the temporary stations near Concordia were provided by Institut Paul-Emile Victor (projects 133 and 906) and Agence Nationale de la Recherche (CASE-IPY, ANR-07-BLAN-0147) associated with the International Polar Year 2007/2008. We also thank the Editor Jeannot Trampert, an anonymous reviewer and Anya M. Reading, who performed a very detailed and constructive review.

REFERENCES

Artemieva, I.M., Billien, M., Lévêque, J.-J. & Mooney, W., 2004. Shear wave velocity, seismic attenuation, and thermal structure of the continental upper mantle, *Geophys. J. Int.,* **157,** 607–628.

Bhattacharyya, J., Masters, G. & Shearer, P., 1996. Global lateral variations of shear wave attenuation in the upper mantle, *J. geophys. Res.,* **101,** 22 273–22 289.

Bijwaard, H., Spakman, W. & Engdahl, E.R., 1998. Closing the gap between regional and global travel time tomography, *J. geophys. Res.,* **103,** 30 055–30 078.

Billien, M., Lévêque, J.-J. & Trampert, J., 2000. Global maps of Rayleigh wave attenuation for periods between 40 and 150 s, *Geophys. Res. Lett.,* **27,** 3619–3622.

Chan, W.W. & Der, Z.A., 1988. Attenuation of multiple *ScS* in various parts of the world, *Geophys. J.,* **92,** 303–314.

Cheng, H.-X. & Kennett, B.L.N., 2002. Frequency dependence of seismic wave attenuation in the upper mantle beneath the Australian region, *Geophys. J. Int.,* **150,** 45–57.

Choudhury, M.A. & Dorel, J., 1973. Spectral ratio of short-period *ScP* and *ScS* phases in relation to the attenuation in the mantle beneath the Tasman Sea and the Antarctic region, *J. geophys. Res*., **78,** 462–469.

Dalton, C.A. & Ekström, G., 2006. Global models of surface wave attenuation, *J. geophys. Res.,* **111,** doi:10.1029/2005JB003997.

Danesi, S. & Morelli, A., 2001. Structure of the upper mantle under the Antarctic plate from surface wave tomography, *Geophys. Res. Lett.,* **28,** 4395–4398

Debayle, E. & Kennett, B.L.N., 2000a. The Australian continental upper mantle: structure and deformation inferred from surface waves, *J. geophys. Res.,* **105,** 25 423–25 450.

Debayle, E. & Kennett, B.L.N., 2000b. Anisotropy in the Australasian upper mantle from Love and Rayleigh waveform inversion, *Earth planet. Sci. Lett.,* **184,** 339–351.

Debayle, E. & Sambridge, M., 2004. Inversion of massive surface wave data sets: model construction and resolution assessment, *J. geophys. Res.,* **109,** doi:10.1029/2003JB002652.

DeMets, C., Gordon, R.G., Argus, D.F. & Stein, S., 1990. Current plate motions, *Geophys. J. Int.,* **101,** 425–478.

Durek, J.J. & Ekström, G., 1996. A radial model of anelasticity consistent with long period surface wave attenuation, *Bull. seism. Soc. Am.,* **86,** 144–158.

Dziewonski, A.M. & Anderson, D.L., 1981. Preliminary reference Earth model, *Phys. Earth planet. Inter.,* **25,** 297–356.

Dziewonski, A.M., Chou, T.A. & Woodhouse, J.H., 1981. Determination of earthquake source parameters from waveform data for studies of global and regional seismicity, *J. geophys. Res.,* **86,** 2825–2852.

Ekström, G., 2007. Global seismicity: results from systematic waveform analyses, 1976–2005, in *Treatise on Geophysics,* Vol. 4, pp. 473–481, ed. Schubert, G., Elsevier, Amsterdam.

Fichtner, A., Kennett, B.L.N., Igel, H. & Bunge, H.-P., 2010. Full waveform tomography for radialy anisotropic structure: new insights into prsent and past states of the Australasian upper mantle, *Earth planet. Sci. Lett.,* **290,** 270–280.

Fishwick, S. & Reading, A.M., 2008. Anomalous lithosphere beneath the Proterozoic of western and central Australia: a record of continental collision and intraplate deformation?, *Precambrian Res.,* **166,** 111–121.

Fishwick, S., Kennett, B.L.N. & Reading, A.M., 2005. Contrasts in lithospheric structure within the Australian craton—insights from surface wave tomography, *Earth planet. Sci. Lett.,* **231,** 163–176.

Flanaghan, M.P. & Wiens, D.A., 1994. Radial upper mantle attenuation structure in inactive back arc basins from differential shear wave measurements, *J. geophys. Res.,* **99,** 15 469–15 485.

Frohlich, C. & Barazangi, M., 1980. A regional study of mantle velocity variations beneath Eastern Australia and the Southwestern Pacific using short-period recordings of *P*, *S*, *PcP*, *ScP* and *ScS* waves produced by Tongan deep earthquakes, *Phys. Earth planet. Inter.,* **21,** 1–14.

Gomer, B.M. & Okal, E.A., 2003. Multiple-ScS probing of the Ontong-Java Plateau, *Phys. Earth planet. Inter.,* **138,** 317–331.

Gung, Y. & Romanowicz, B., 2004. *Q* tomography of the upper mantle using three-component long-period waveforms, *Geophys. J. Int,* **157,** 813–830.

Gurnis, M., Müller, R.D. & Moresi, L., 1998. Cretaceous vertical motion of Australia and the Australian-Antarctic Discordance, *Science,* **279,** 1499–1504.

Jordan, T.H. & Sipkin, S.A., 1977. Estimation of the attenuation operator for multiple *ScS* waves, *Geophys. Res. Lett.,* **4,** 167–170.

Lawrence, J.F. & Wysession, M.E., 2006. QLM9: A new radial quality factor (Q) model for the lower mantle, *Earth planet. Sci. Lett.,* **241,** 962–971.

Lawrence, J.F. & Wysession, M.E., 2006. Seismic evidence for Subduction-Transported water in the lower mantle, in *Earth's Deep Water Cycle,* Geophys. Monograph 168, pp. 251–261, eds Jacobsen, S.D. & van der Lee, American Geophysical Union, Washington, DC.

Lay, T. & Wallace, T.C., 1983. Multiple *ScS* attenuation beneath Mexico and Central America, *Geophys. Res. Lett.,* **10,** 301–304.

Lay, T. & Wallace, T.C., 1988. Multiple *ScS* attenuation and travel times beneath Western North America, *Bull. seism. Soc. Am.,* **78,** 2041–2061.

Lekić, V. & Romanowicz, B., 2011. Inferring upper-mantle structure by full waveform tomography with the spectral element method, *Geophys. J. Int.,* **185,** 799–831

Lévêque, J.J., Maggi, A., Delladio, A., Burdin, J., Thore, J.Y. & Morelli, A., 2008. *ConCorDia: A New, Permanent Seismological Station in Antarctica,* EGU General Assembly, Vienna, Austria.

Levêque, J.J., Maggi, A. & Souriau, A., 2010. Seismological constraints on ice properties at Dome C, Antarctica, from horizontal to vertical spectral ratios, *Antarctic Sci.,* **22,** 1–8, doi:10.1017/S0954102010000325.

Maggi, A. & Lévêque, J.J., 2010. Des stations sismologiques en Antarctique: enjeux globaux et locaux, in *Rapport d'activité 2008 de l'Institut polaire français Paul-Emile Victor,* pp. 22–23, IPEV, Plouzané, France.

Masters, G., Barmine, M. & Kientz, S., 2011. Mineos user manual Version 1.0.2. Available at: http://www.geodynamics.org/cig/software/mineos/mineos.pdf, 97pp. (last accessed 2011 September).

Nakanishi, I., 1979. Attenuation of multiple *ScS* waves beneath the Japanese arc, *Phys. Earth planet. Inter.,* **19,** 337–347.

Reading, A.M. & Heintz, M., 2008. Seismic anisotropy of East Antarctica from shear-wave splitting: spatially varying contributions from lithospheric structural fabric and mantle flow?, *Earth planet. Sci. Lett.,* **268,** 433–443.

Reid, F.J.L., Woodhouse, J.H. & van Heijst, H.J., 2001. Upper mantle attenuation and velocity structure from measurements of differential *S* phases, *Geophys. J. Int.,* **145,** 615–630.

Ritzwoller, M.H., Shapiro, N.M. & Leahy, G.M., 2003. A resolved mantle anomaly as the cause of the Australian-Antarctic Discordance, *J. geophys. Res.,* **108,** B12, doi:10.1029/2003JB002522.

Romanowicz, B., 1998. Attenuation tomography of the Earth's mantle: a review of current status, *Pure appl. Geophys.,* **153,** 257–272.

Romanowicz, B. & Mitchell, B.J., 2007. Deep Earth structure – *Q* of the Earth from crust to core, in *Treatise on Geophysics,* Vol. 1, pp. 731–774, ed. Schubert, G., Elsevier, Amsterdam.

Selby, N.D. & Woodhouse, J.H., 2002. The *Q* structure of the upper mantle: constraints from Rayleigh wave amplitudes, *J. geophys. Res.,* **107,** doi:10.1029/2001JB00257.

Sieminski, A., Debayle, E. & Lévêque, J.J., 2003. Seismic evidence for deep low-velocity anomalies in the transition zone beneath West Antarctica, *Earth planet. Sci. Lett.,* **216,** 645–661.

Van der Hilst, R., 1995. Complex morphology of subducted lithosphere in the mantle beneath the Tonga trench, *Nature,* **374,** 154–157.

Whittaker, J.M., Müller, R.D. & Gurnis, M., 2010. Development of the Australian-Antarctic depth anomaly, *Geochem. Geophys. Geosyst.,* **11,** doi:10.1029/2010GC003276.